Complex Permittivity Imaging by Incorporating Synthetic Aperture Radar and Inverse Scattering Method for Stratified Ground Medium

Yoshihiro Yamauchi and Shouhei Kidera [ID], *Senior Member, IEEE*

Abstract—This article introduces the incorporationapproach with synthetic aperture radar (SAR) and contrast source inversion (CSI) based nonlinear inverse scattering (NIS) approach for quantitative permittivity imaging for buried object under multilayered heterogeneous ground media. It is challenging issue to retrieve a complex permittivity from ground-penetrating radar (GPR) data, since the NIS problem considerably suffers from inaccuracy due to severe ill-posed condition. To overcome this limitation, this article introduces the SAR image-based region of interest (ROI) limitation in the CSI optimization scheme, where the number of unknowns are massively reduced. Furthermore, the SAR image is also upgraded by the pre-CSI optimization, where the Green's function and background clutter for heterogeneous background (e.g., multilayered medium) are accurately generated. The FDTD-based numerical tests, assuming GPR observation model, show that our proposed scheme effectively reconstructs a dielectric property of buried object, even in severe condition.

Index Terms—Complex permittivity, contrast source inversion (CSI) method, ground-penetrating radar (GPR), microwave subsurface imaging, nonlinear inverse scattering (NIS), synthetic aperture radar (SAR).

I. INTRODUCTION

THERE is a growing demand for effective monitoring tools for underground and subsurface investigations. Ground-penetrating radar (GPR) is used for soil structure analysis and detecting anomalies, such as air voids and water leakage in sewage systems. This is important as these anomalies can cause devastating disasters, especially during earthquakes or excavation for tunnels or roads [1]. In addition, monitoring transportation infrastructure, such as highways, bridges, or tunnels, is critical to prevent catastrophic collapse due to aging. Microwave GPR is a promising option for reliable investigation, providing deep penetration depth of meters and high range and azimuth resolution through ultrawideband (UWB) signal and synthetic aperture processing.

Synthetic aperture radar (SAR) processing is an efficient imaging scheme assuming GPR observations [2], [3]. It can

provide a reflectivity coefficient for a buried object with high azimuth resolution by integrating the reflection signal coherently under a phase compensation of the propagation delay [4], [5], [6]. However, SAR can only offer a qualitative profile, making it difficult to discriminate the physical, chemical, or electrical characteristics of a buried material, such as air, water, brine, or other compounds. In addition, in cases where the background soil medium has a heterogeneous profile, such as a multilayered structure, SAR images may suffer from inaccuracy due to an inappropriate propagation model or multiple scattering among stratified layers. More critical point is that the image accuracy largely depends on the selected permittivity value, which determines the propagation speed and is difficult to determine as it varies in a heterogeneous background model. Some studies have attempted to address this difficulty [6], [7], but they still could not resolve unnecessary responses due to multiple scattering effects or other clutter responses.

To address this issue, we previously proposed the nonlinear inverse scattering (NIS) enhanced SAR approach [8], [9], where the contrast source inversion (CSI) NIS scheme is introduced to achieve an accurate propagation function, such as Green's function, and suppress clutter response by exploiting the optimal outputs of the CSI. While this scheme successfully enhances the reconstruction accuracy of the SAR image in the stratified media, it still has an substantial issue that the dielectric properties of an object could not be retrieved.

To solve this problem, this article introduces the NIS approach in the GPR model to retrieve a complex permittivity value by exploiting the SAR image obtained by the method. There have been various studies on quantitative reconstruction using the NIS method. The diffraction tomography-based reconstruction, which is a linear Born approximation, has been introduced in several literatures [10], [11], [12]. However, it suffers from inaccuracy for high-contrast objects like water or air voids due to nonlinearity. On the other hand, NIS-based multiresolution [13], [14], [15] or Bayesian compression techniques [16], [17] have been implemented successfully by reducing the number of unknowns or introducing a sparse regularization scheme. However, the abovementioned approaches require an iterative use of forward solver, such as FDTD method, and needs significantly expensive computational cost. Nonetheless, these approaches require iterative use of a forward solver like the FDTD method, which is computationally expensive. In contrast, the CSI [18], [19], [20] has been widely used in many applications, including

the GPR model [21], [22], [23], [24], [25], due to its cost effective inversion scheme that optimizes the total field in the region of interest (ROI) without recursive calculation of the forward problem. Building on the CSI feature, we have proposed the CSI-based permittivity extraction for multilayered media [26], where the CSI cost function evaluates the possible combination of relative permittivity. Another notable CSI feature is that it provides both a contrast function (dielectric profile as primary variables) and a total field in the ROI (secondary variables), enabling the determination of the Green's function for the assumed heterogeneous background media. However, the CSI suffers from the ill-posed feature, which is more severe in the GPR model due to the limited illumination angle. Some literature has introduced radar-image-based ROI restriction [27], [28], [29], [30], [31], [32], where the ROI is focused on the area where the target exists. Nevertheless, the accuracy of the ROI is essential to determine the actual target area. Therefore, we introduced the CSI-enhanced SAR image by the method [8], [9] to enhance the reconstruction accuracy of the CSI reconstruction.

Notably, the CSI necessitates not only the Green's function for the interaction between the sensor and the ROI, but also for all the potential pairings of two different locations within the ROI. These could not be supplied by the CSI updating scheme. To maintain accuracy even in a heterogeneous background, we introduce an approximated Green's function model that assumes a homogeneous profile with an average dielectric property.

The main contributions of this study, namely the bidirectional processing between radar and tomography, are as follows.

1) *Tomography → Radar:* We use the CSI optimization variables, regarding the total field, to generate accurate Green's functions for heterogeneous media. We also use them to reconstruct unnecessary clutter response caused by reflection from background heterogeneity.
2) *Radar → Tomography:* We introduce the CSI-enhanced SAR for prior ROI estimation in post-CSI-based permittivity reconstruction. This significantly reduces the number of unknowns.
3) The Green's function defined in the data equation is used in the ROI limitation scheme, to avoid using the forward solver. The Green's function in the state equation is approximated to the analytical Green's function with homogeneous assumption.

Our proposed scheme shows effective ROI estimation in multilayered background media and attains a more accurate dielectric profile by post-CSI reconstruction in both permittivity and conductivity, even in severe ill-posed conditions. We demonstrate these results through a two-dimensional FDTD-based numerical test, assuming a stratified soil structure with a C-band GPR model.

II. METHOD

A. Observation Model

The observation model, shown in Fig. 1, assumes a multilayered ground media including a buried object. The locations of the transmitter and receiver are defined as r_T and r_R, respectively, and the observation area, including the scanning line,
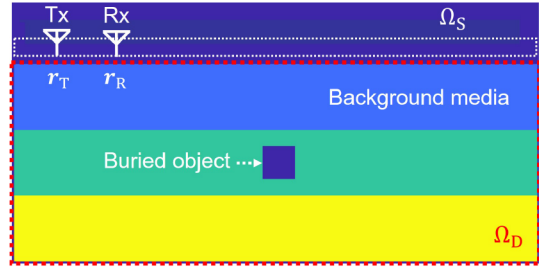

Fig. 1. Observation model, assuming multilayered ground media, including buried object.

is defined as the domain Ω_S. The background medium forms a multilayered structure, with each layer having a consistent dielectric property. $E^T(\omega; r_T, r_R)$ denotes the total electric field measured at the receiver r_R with the angular frequency ω, when the incident field is illuminated by the transmitter at r_T. We defined the scattered electric field as $E^S(\omega; r_T, r_R) \equiv E^T(\omega; r_T, r_R) - E^I(\omega; r_T, r_R)$, where $E^I(\omega; r_T, r_R)$ denotes the incident electric field. The ROI is defined as Ω_D, which depends on the definition of the background media.

B. Contrast Source Inversion

For GPR applications, radar imaging techniques, such as SAR or range migration schemes have been widely used to provide the location or shape of buried objects. However, these techniques face a critical problem in that they cannot retrieve complex permittivity values as a quantitative metric. This limitation makes it difficult to recognize the materials of buried objects, such as air voids, or water-filled objects. In addition, in the case of multiple background layer media, the reconstruction accuracy of the radar image depends heavily on the selected propagation model, especially for the relative permittivity of the background media, which is usually assumed to be homogeneous.

To address these issues, we introduce a CSI-based complex permittivity retrieval approach for objects under multilayered ground media. CSI is one of the most promising inverse scattering methods that can reconstruct a dielectric profile without the need for iterative calculations by a forward solver [18]. The methodology is briefly described as follows: first, the scattered electric field $E^S(\omega; r_T, r_R)$ can be expressed as the following domain integral equation:

$$E^S(\omega; r_T, r_R) = k_B^2 \int_{\Omega_D} G^B(\omega; r, r_R) w(\omega; r_T, r) dr \quad (1)$$

where k_B and $G^B(\omega; r, r_R)$ denote the wave number and Green's function of the assumed background media, respectively. $\chi(\omega; r) \equiv (\epsilon(r) - \epsilon_B(r))/\epsilon_B(r)$ denotes the contrast function, where $\epsilon(r)$ and $\epsilon_B(r)$ are complex permittivities at r with and without an object, respectively. $w(\omega; r_T, r) \equiv \chi(\omega; r) E^T(\omega; r_T, r)$ is called the contrast source. It should be noted that (1) is expected to hold true in the domains Ω_S and Ω_D, which are referred to as the data and state equations, respectively.

The CSI method introduces a cost function that takes into account two physical constraints, (1) in Ω_S and Ω_D. The cost

function is defined as

$$F(\chi, w) \equiv \frac{\sum_{\boldsymbol{r}_T} \|E^S(\omega; \boldsymbol{r}_T, \boldsymbol{r}_R) - \mathcal{G}^S[w]\|_{\Omega_S}^2}{\sum_{\boldsymbol{r}_T} \|E^S(\omega; \boldsymbol{r}_T, \boldsymbol{r}_R)\|_{\Omega_S}^2}$$

$$+ \lambda \frac{\sum_{\boldsymbol{r}_T} \left\| \begin{array}{c} \chi(\omega; \boldsymbol{r})E^I(\omega; \boldsymbol{r}_T, \boldsymbol{r}') \\ -w(\omega; \boldsymbol{r}_T, \boldsymbol{r}) + \chi(\omega; \boldsymbol{r})\mathcal{G}^D[w] \end{array} \right\|_{\Omega_D}^2}{\sum_{\boldsymbol{r}_T} \|\chi(\omega; \boldsymbol{r})E^I(\omega; \boldsymbol{r}_T, \boldsymbol{r}')\|_{\Omega_D}^2}.$$

$$(2)$$

Here, λ is the regularization coefficient, and the operators $\mathcal{G}^S$ and $\mathcal{G}^D$ are defined as

$$\mathcal{G}^S[w] = k_B^2 \int_{\Omega_D} G^B(\omega; \boldsymbol{r}_R, \boldsymbol{r})w(\omega; \boldsymbol{r}_T, \boldsymbol{r})d\boldsymbol{r}, \, (\boldsymbol{r}_R \in \Omega_S)$$

$$(3)$$

$$\mathcal{G}^D[w] = k_B^2 \int_{\Omega_D} G^B(\omega; \boldsymbol{r}', \boldsymbol{r})w(\omega; \boldsymbol{r}_T, \boldsymbol{r})d\boldsymbol{r}, \, (\boldsymbol{r}' \in \Omega_D) \quad (4)$$

where $\|\cdot\|_{\Omega_S}^2$ and $\|\cdot\|_{\Omega_D}^2$ denote the l_2 norms calculated in Ω_S and Ω_D, respectively. The three variables, $w(\boldsymbol{r}_T, \boldsymbol{r})$, $E^T(\omega; \boldsymbol{r}_T, \boldsymbol{r})$, and $\chi(\omega; \boldsymbol{r})$ with $\boldsymbol{r} \in \Omega_D$, are sequentially updated to minimize the cost function (2). Note that the Green's function denoted as $G^B(\omega; \boldsymbol{r}_R, \boldsymbol{r})$ or $G^B(\omega; \boldsymbol{r}', \boldsymbol{r})$ represents the generic versions of the Green's functions, which do not indicate a specific background. The CSI has a distinct computational advantage in that it does not require iterative calculations of the forward solver, such as FDTD, since the total field $E^T(\omega; \boldsymbol{r}_T, \boldsymbol{r})$ in the ROI is sequentially updated in the optimization sequence.

However, in a general GPR model, the CSI or other inverse scattering approaches suffer from an inherent problem: an ill-posed condition. This is because the illumination angle from the source is severely limited in the GPR model, and the number of observation data is much less than that of the unknowns. To address this issue, the radar prior-based CSI has been developed in [27]. This method drastically reduces the number of unknowns by limiting the ROI using a radar image. Nevertheless, the reconstruction accuracy of the complex permittivity depends largely on the given radar image, which can suffer from inaccuracy in multiple background media because the major radar approach assumes homogeneous single-layered media.

C. CSI Enhanced CI

Based on the discussions mentioned earlier, it is clear that we require an accurate radar imaging scheme for multiple-layered models. To achieve this accuracy, we need to estimate the Green's function from the transmitter to the imaging point (all points included in ROI) and to the receiver in a heterogeneous background. However, these Green's functions are not typically expressed in an analytical form and needed to be calculated using forward solvers, such as FDTD. These solvers, however, necessitate significant computational resources.

In order to address these issues, our previous study [8] proposed a CSI-enhanced radar imaging scheme that is highly compatible with post-CSI processing. Here, we briefly describe the methodology of this method. One of the key features of the CSI is that it can optimize not only the estimated contrast
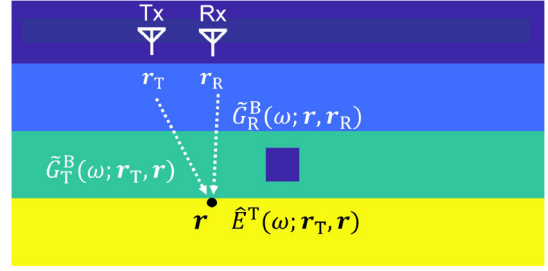

Fig. 2. Illustration for Green's functions in (5) and (6) for CSI enhanced CI processing.

function $\hat{\chi}$ but the total field in the ROI as $\hat{E}^T(\omega; \boldsymbol{r}_T, \boldsymbol{r})$, as the final optimization outputs. Given a contrast function χ_{bg} of the multilayer background (excluding the buried object), we only updated the total field, denoted as $\hat{E}^T(\omega; \boldsymbol{r}_T, \boldsymbol{r})$ with a fixed χ_{bg}. In this case, the Green's functions in (3) and (4) are defined as those in free space.

Given that the Green's functions for stratified background media needed for the post-CI process are seldom provided in an analytical form, they were determined using the following equations as described in [8], [9], and [33]:

$$\tilde{G}_T^B(\omega; \boldsymbol{r}_T, \boldsymbol{r}) \equiv \frac{\hat{E}^T(\omega; \boldsymbol{r}_T, \boldsymbol{r})}{E_{air}^T(\omega; \boldsymbol{r}_T, \boldsymbol{r}_T)} \quad (5)$$

$$\tilde{G}_R^B(\omega; \boldsymbol{r}_R, \boldsymbol{r}) \equiv \frac{\hat{E}^T(\omega; \boldsymbol{r}_R, \boldsymbol{r})}{E_{air}^T(\omega; \boldsymbol{r}_R, \boldsymbol{r}_R)} \quad (6)$$

where $E_{air}^T(\omega; \boldsymbol{r}_T, \boldsymbol{r}_T)$ and $E_{air}^T(\omega; \boldsymbol{r}_R, \boldsymbol{r}_R)$ are the total fields from the source located at $\boldsymbol{r}_T$ and observed at $\boldsymbol{r}_R$, respectively, assuming the background media is vacuum. $\hat{E}^T(\omega; \boldsymbol{r}_T, \boldsymbol{r})$ and $\hat{E}^T(\omega; \boldsymbol{r}_R, \boldsymbol{r})$ denote the total fields at $\boldsymbol{r} \in \Omega_D$ that are optimized by the pre-CSI process. Fig. 2 provides a physical representation of the Green's functions presented in (5) and (6). Under the reciprocal theory and mono-static configuration, both $\hat{E}^T(\omega; \boldsymbol{r}_T, \boldsymbol{r})$ and $\hat{E}^T(\omega; \boldsymbol{r}_R, \boldsymbol{r})$ are available. Note that this method provides an accurate propagation model in the heterogeneous background as the Green's functions in (5) and (6) are determined by exploiting the optimized output of the CSI, without requiring any calculation of the forward solver. Finally, the radar image $\tilde{I}(\boldsymbol{r})$ using the following equation:

$$\tilde{I}(\boldsymbol{r}) = \sum_{(\boldsymbol{r}_T, \boldsymbol{r}_R) \in \Omega_S} \int_{-\infty}^{\infty} \tilde{E}^S(\omega; \boldsymbol{r}_T, \boldsymbol{r}_R)$$

$$\times \tilde{G}_R^B(\omega; \boldsymbol{r}_R, \boldsymbol{r})\tilde{G}_T^{B*}(\omega; \boldsymbol{r}_T, \boldsymbol{r})d\omega \quad (7)$$

where $\tilde{E}^S(\omega; \boldsymbol{r}_T, \boldsymbol{r}_R) \equiv E^T(\omega; \boldsymbol{r}_T, \boldsymbol{r}_R) - \tilde{E}^{TB}(\omega; \boldsymbol{r}_T, \boldsymbol{r}_R)$, is defined where $\tilde{E}^{TB}(\omega; \boldsymbol{r}_T, \boldsymbol{r}_R)$ is the total field in the case of a background multilayered medium without a buried object.

Subsequently, to provide a suitable $\tilde{E}^S(\omega; \boldsymbol{r}_T, \boldsymbol{r}_R)$, the total fields sourced solely from the stratified background media are generated. This was done to reconstruct the CI image solely for the buried object as indicated in (7). We were particularly interested in the CSI characteristic that supplies the total field in the ROI. This allowed us to generate the total fields from the
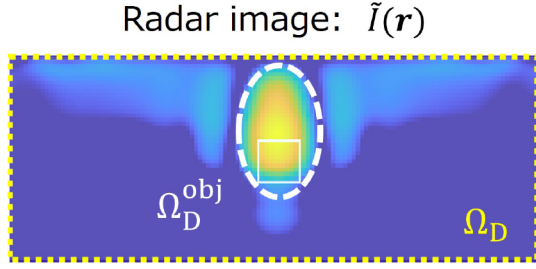
Fig. 3. Radar image-based ROI limitation scheme in the proposed method.

background clutter responses (scattered responses excluding the buried object) at the observation area Ω_S as $\tilde{E}^{TB}(\omega; \boldsymbol{r}_T, \boldsymbol{r}_R)$

$$
\tilde{E}^{TB}(\omega; \boldsymbol{r}_T, \boldsymbol{r}_R) \equiv E^I(\omega; \boldsymbol{r}_T, \boldsymbol{r}_R)
$$
$$
+ k_B^2 \int_{\Omega_D} G_{air}^B(\omega; \boldsymbol{r}_R, \boldsymbol{r}) \tilde{w}(\omega; \boldsymbol{r}_T, \boldsymbol{r}) d\boldsymbol{r}
$$
$$
(\boldsymbol{r}_R \in \Omega_S). \tag{8}
$$

In this scenario, $G_{air}^B(\omega; \boldsymbol{r}_R, \boldsymbol{r})$ is the Green's function in free space, and $\tilde{w}(\omega; \boldsymbol{r}_T, \boldsymbol{r}) \equiv \hat{\chi}(\omega, \boldsymbol{r}) \hat{E}^T(\omega; \boldsymbol{r}_T, \boldsymbol{r})$ is defined. Herein, $\hat{\chi}(\omega, \boldsymbol{r})$ represents the contrast function of the assumed stratified background. This process aligns with the "tomography → radar" processing. By calculating (8), we could produce a scattered response $\tilde{E}^S(\omega; \boldsymbol{r}_T, \boldsymbol{r}_R)$ that excludes the background responses from the stratified media.

D. Radar-Based ROI Limitation for CSI

To achieve accurate reconstruction of the complex permittivity of buried objects, this article introduces a radar image-based ROI limitation for post-CSI reconstruction. In this method, the CSI-enhanced radar image, $\tilde{I}(\boldsymbol{r})$, is used to determine the ROI, which includes the object as Ω_D^{obj}

$$
\Omega_D^{obj} = \{\boldsymbol{r} \mid |\tilde{I}(\boldsymbol{r})| \geq \alpha \max_{\boldsymbol{r}} |\tilde{I}(\boldsymbol{r})|\} \tag{9}
$$

where α is a constant threshold with $0 \leq \alpha \leq 1$. Fig. 3 shows the illustration of the radar image-based ROI limitation scheme.

To introduce the ROI limitation scheme for the post-CSI process, we need to define the Green's function for the multilayered background media. Considering the Green's function of the data equation in (3) as $G^B(\omega; \boldsymbol{r}_R, \boldsymbol{r})$, it can be obtained by the pre-CSI outputs as

$$
\tilde{G}_R^B(\omega; \boldsymbol{r}_R, \boldsymbol{r}) \equiv \frac{\hat{E}^T(\omega; \boldsymbol{r}_R, \boldsymbol{r})}{E_{air}^T(\omega; \boldsymbol{r}_R, \boldsymbol{r}_R)}. \tag{10}
$$

This approach is similar to (5) and (6). However, in the state equation in (4), the Green's function $G^B(\omega; \boldsymbol{r}', \boldsymbol{r})$ is not provided by the CSI optimization process, as it necessitates defining for all possible cell combinations within the assumed ROI. To address this issue, we assume that the background medium in the limited ROI possesses homogeneous properties, such as the average profile of stratified media. In this context, we introduce the
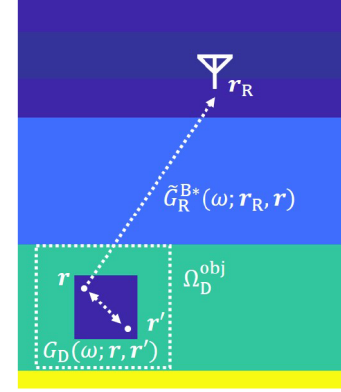

Fig. 4. Green's function in the ROI.

following Green's function for the state (6):

$$
\tilde{G}^B(\omega; \boldsymbol{r}', \boldsymbol{r}) = -\frac{i}{4} H_0^{(2)}(k_B |\boldsymbol{r} - \boldsymbol{r}'|), (\boldsymbol{r}, \boldsymbol{r}' \in \Omega_D) \tag{11}
$$

where k_B represents the wavenumber of the background medium, typically determined by the average dielectric properties of the stratified media within the limited ROI. $H_0^{(2)}$ expresses the Hankel function of the second kind and zeroth order. Then, we redefine the cost function of the post-CSI as

$$
F(w, \chi) \equiv \sum_\omega \frac{\sum_{\boldsymbol{r}_T} \|\tilde{E}^S(\omega; \boldsymbol{r}_T, \boldsymbol{r}_R) - \tilde{\mathcal{G}}^S[w]\|_{\Omega_S}^2}{\sum_{\boldsymbol{r}_T} \|\tilde{E}^S(\omega; \boldsymbol{r}_T, \boldsymbol{r}_R)\|_{\Omega_S}^2}
$$
$$
+ \sum_\omega \frac{\sum_{\boldsymbol{r}_T} \|\chi(\omega; \boldsymbol{r})\hat{E}^T(\omega; \boldsymbol{r}_T, \boldsymbol{r}) - w(\omega; \boldsymbol{r}_T, \boldsymbol{r}) + \chi(\omega; \boldsymbol{r})\tilde{\mathcal{G}}^D[w]\|_{\Omega_D^{obj}}^2}{\sum_{\boldsymbol{r}_T} \|\chi(\omega; \boldsymbol{r})\hat{E}^T(\omega; \boldsymbol{r}_T, \boldsymbol{r})\|_{\Omega_D^{obj}}^2}. \tag{12}
$$

Here, the operators $\tilde{\mathcal{G}}^S[w]$ and $\tilde{\mathcal{G}}^D[w]$ are defined as

$$
\tilde{\mathcal{G}}^S[w] = k_B^2 \int_{\Omega_D^{obj}} \tilde{G}_R^{B*}(\omega; \boldsymbol{r}_R, \boldsymbol{r}') w(\omega; \boldsymbol{r}_T, \boldsymbol{r}') d\boldsymbol{r}' \tag{13}
$$

$$
\tilde{\mathcal{G}}^D[w] = k_B^2 \int_{\Omega_D^{obj}} \tilde{G}^B(\omega; \boldsymbol{r}', \boldsymbol{r}) w(\omega; \boldsymbol{r}_T, \boldsymbol{r}) d\boldsymbol{r}'. \tag{14}
$$

Fig. 4 depicts the Green's function model utilized in this method, which offers several advantages. One of the significant benefits is that it can improve the accuracy of complex permittivity reconstruction within the limited ROI by drastically reducing the number of unknowns. Moreover, this method considerably decreases the computational complexity, eliminating the need for the forward solver-based calculation of the Green's function in both the data and state equations.

E. Procedure of Proposed Method

The processing flow of the proposed method is summarized as follows.

Step 1) The dielectric profile of the background media, e.g., multilayered media, is obtained by a prior knowledge or other estimation method, like [26].

TABLE I
DEFINITIONS AND ROLES OF GREEN'S FUNCTIONS USED IN THE PROPOSED METHOD

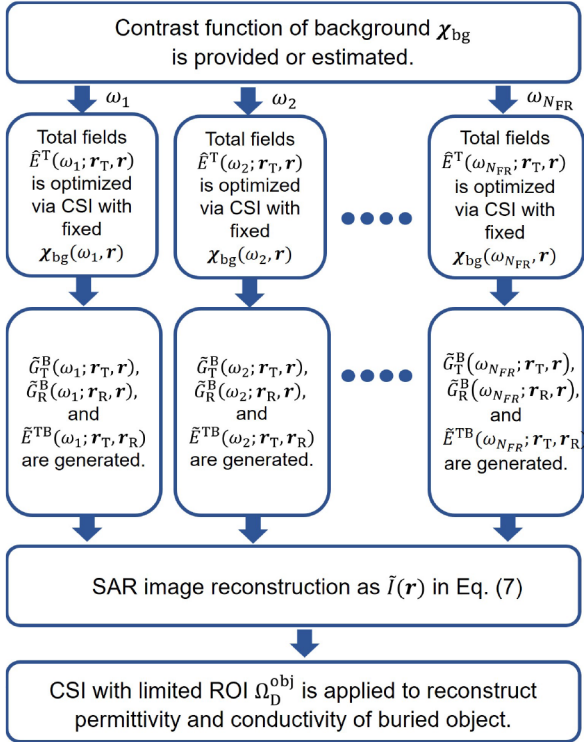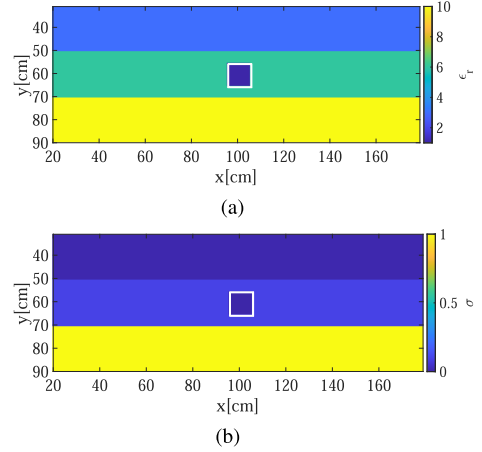| Notations	Definitions	Background media	Roles
$\tilde{G}_{\mathrm{T}}^{\mathrm{B}}(\omega; \boldsymbol{r}_{\mathrm{T}}, \boldsymbol{r})$ $\tilde{G}_{\mathrm{R}}^{\mathrm{B}}(\omega; \boldsymbol{r}_{\mathrm{R}}, \boldsymbol{r})$	(5) and (6)	Stratified media	Generating propagation model in stratified media in CSI-Enhanced CI in (7)
$G_{\mathrm{air}}^{\mathrm{B}}(\omega; \boldsymbol{r}_{\mathrm{R}}, \boldsymbol{r})$	(8)	Free space	Used for clutter suppression from stratified media in (8)
$\tilde{G}_{\mathrm{R}}^{\mathrm{B}}(\omega; \boldsymbol{r}_{\mathrm{R}}, \boldsymbol{r})$	(10)	Stratified media	Used for data equation [see (13)] for generating the cost function in (12)
$\tilde{G}^{\mathrm{B}}(\omega; \boldsymbol{r}', \boldsymbol{r})$	(11)	Homogeneous media (Average of stratified media)	Used for state equation [see (14)] for generating the cost function in (12)

Fig. 5. Processing of the proposed method.

Fig. 6. Ground truth profiles for relative permittivity and conductivity in Case 1. (a) Permittivity. (b) Conductivity.

method, as outlined in (5), (8), (10), and (11), we provide a summary of their definitions and roles in Table I.

III. RESULTS: FDTD NUMERICAL TEST

A. Numerical Setting

This section presents the 2-D FDTD numerical tests, which assume GPR for a multilayer ground medium. Herein, we presume mono-static configuration, where the transmitter and receiver are located in the same place. We consider three planar ground layers located in the vacuum: the first, second, and third layers model dry, humid, and saturated clay, respectively, with each dielectric property referred from the literature [34]. We assume the two types of buried objects. We assume two types of buried objects: an air void, named as Case 1, and a wet clay, categorized as Case 2. Figs. 6 and 7 show the target cases for Cases 1 and 2, respectively, and Table II shows the dielectric parameters and dimensions of each layer and buried object. We perform a scan using a set of transmitters and receivers located at the same position along the straight line of $y = 200$ mm, spaced at 100 mm intervals. This spacing should be shorter than the center wavelength in the second layer, which was 211 mm, to avoid a grating lobe effect. The total number of observation points, as a result, is 17. We assume the L-band GPR radar model, which has a center frequency of 0.58 GHz and a bandwidth of 0.37 GHz. The theoretical determination of the

And this contrast function is defined as $\chi_{\mathrm{bg}} \equiv (\chi_1, \ldots, \chi_n, \ldots, \chi_{N_{\mathrm{layer}}})$.

Step 2) The total field in the ROI as $\hat{E}^{\mathrm{T}}(\omega_i; \boldsymbol{r}_{\mathrm{T}}, \boldsymbol{r})$ is updated for each angular frequency ω_i, using CSI with fixed $\chi(\omega_i, \boldsymbol{r})$ determined by χ_{bg}, where the Green's function in free space is used.

Step 3) The Green's functions $\tilde{G}_{\mathrm{T}}^{\mathrm{B}}(\omega_i; \boldsymbol{r}_{\mathrm{T}}, \boldsymbol{r})$ and $\tilde{G}_{\mathrm{R}}^{\mathrm{B}}(\omega_i; \boldsymbol{r}_{\mathrm{R}}, \boldsymbol{r})$ are calculated in (5) and (6), respectively, and $\tilde{E}^{\mathrm{TB}}(\omega_i; \boldsymbol{r}_{\mathrm{T}}, \boldsymbol{r}_{\mathrm{R}})$ is calculated using (8). Then, the CSI-enhanced radar image is calculated as $\tilde{I}(\boldsymbol{r})$ using (7).

Step 4) The limited ROI is determined as $\Omega_{\mathrm{D}}^{\mathrm{obj}}$ in (9) and the post-CSI process is performed to minimize the cost function and obtain the final reconstruction profile of the buried object.

Fig. 5 shows the flowchart of the proposed method. Given that there are various definitions of Green's functions in our proposed

TABLE II
DIELECTRIC PARAMETER FOR EACH LAYER AND OBJECT

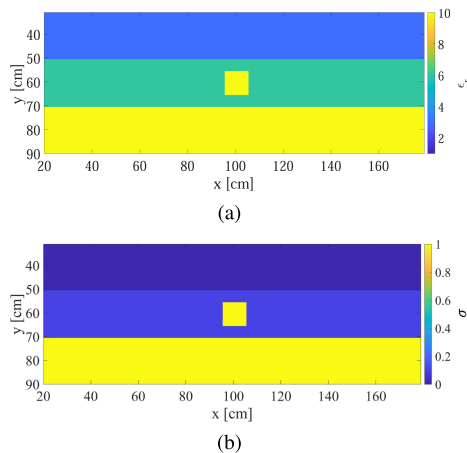|	Relative permittivity	Conductivity [S/m]	Dimensions [mm]
Background	1.0	0	-
First layer	3.0	0.01	1600 mm × 200 mm
Second layer	6.0	0.1	1600 mm × 200 mm
Third layer	10.0	1.0	1600 mm × 200 mm
Object (Case 1)	1.0	0	100 mm × 100 mm
Object (Case 2)	10.0	1.0	100 mm × 100 mm

(a)

(b)

Fig. 7. Ground truth profiles for relative permittivity and conductivity in Case 2. (a) Permittivity. (b) Conductivity.

(a)

(b)

Fig. 8. Reconstruction results of each SAR method in Case 1. (a) Conventional SAR. (b) CSI enhanced SAR.
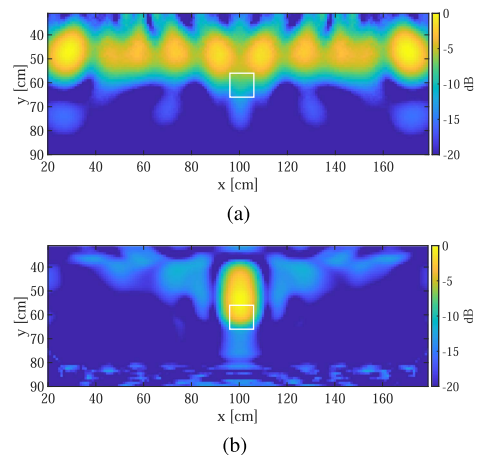

(a)

(b)

Fig. 9. Reconstruction results of each SAR method in Case 2. (a) Conventional SAR. (b) CSI enhanced SAR.

range and cross-range resolutions of SAR image is dependent on parameters, such as bandwidth, center wavelength, and synthetic aperture length. Specifically, at a depth of 40 cm with $\epsilon_B = 6$, the range and cross-range resolutions are 76 mm and 53 mm, respectively. We set the cell sizes for the FDTD, radar image, and CSI inversion to 10 mm, which is less than 1/10 wavelength in the third layer, which is 163 mm. For the processing of SAR or CSI, we utilize 59 frequency samples within the 10 dB bandwidth. Notably, a spatial resolution of the CSI is defined as the size of the inversion cell, which is 10 mm.

B. Results: Radar Image Reconstruction

First, we present the reconstruction results obtained through the radar-based imaging method described in Section II-C, which is referred to as the conventional SAR in [8]. Figs. 8 and 9 show the reconstruction images obtained through the conventional SAR and the CSI-enhanced SAR approaches. In the conventional SAR approach, the background medium is assumed to be homogeneous with a constant permittivity, denoted as ϵ_B, with the surface reflection from the first layer eliminated. In this case, a value of $\epsilon_B = 3.0$ is set for the conventional SAR approach. The results indicate that the conventional SAR approach suffers from significant clutter responses from the second or third layers, and it cannot accurately locate the actual buried object in either case. Moreover, even if we eliminate the clutter responses caused by the heterogeneity of the background media, the reconstruction image heavily depends on the selected relative
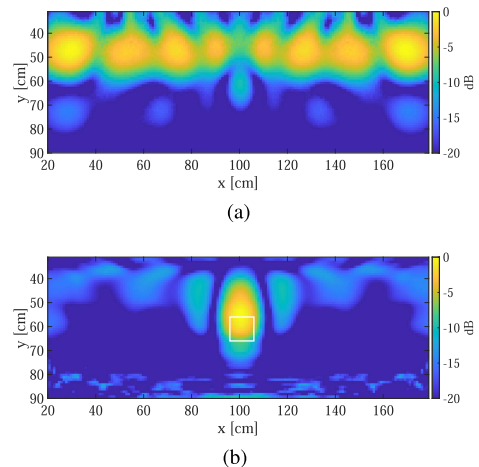
permittivity, ϵ_B. This dependence poses a critical challenge when an inappropriate relative permittivity is selected, or when dealing with cases involving multiple objects located in different layers. On the other hand, the CSI-enhanced SAR approach can accurately locate and shape the buried object to a certain extent. These images focus on the center of the upper surface, as reflections occur on the upper surface of the buried object. Furthermore, the CSI-enhanced SAR approach avoids unnecessary
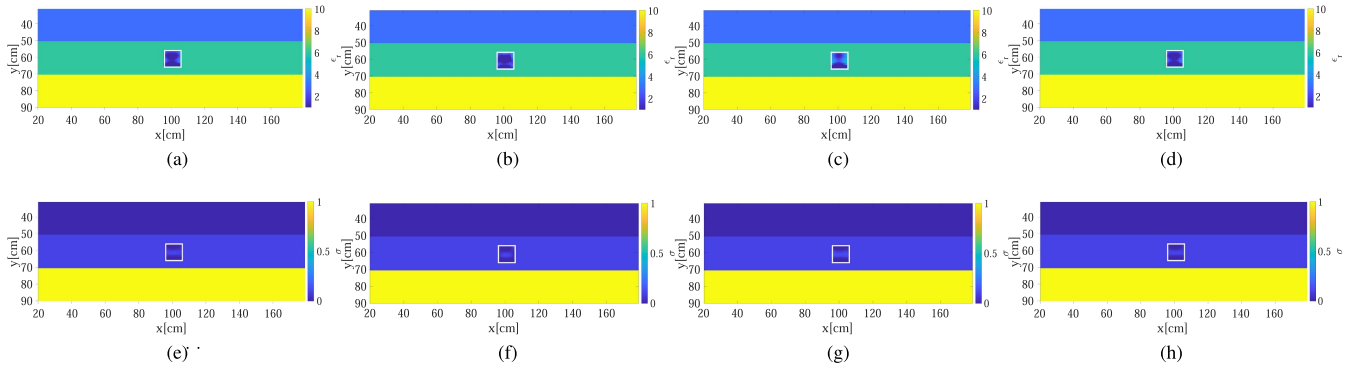
Fig. 10. Reconstruction results using each condition, assuming Case 1 object. First line: Relative permittivity. Second line: Conductivity. (a) Condition I. (b) Condition II. (c) Condition III. (d) Condition IV. (e) Condition I. (f) Condition II. (g) Condition III. (h) Condition IV.

TABLE III
CONDITIONS FOR GREEN'S FUNCTION

Condition	Green's func. in (3) Data Eq.	Green's func. in (4) State Eq.
Condition I	FDTD	FDTD
Condition II	CSI	FDTD
Condition III	FDTD	Hankel Func.
Condition IV	CSI	Hankel Func.

TABLE IV
RMSE FOR PERMITTIVITY AND CONDUCTIVITY UNDER EACH CONDITION OF
GREEN'S FUNCTION

	RMSE_ϵ	RMSE_σ S/m
Condition I	2.63	0.07
Condition II	2.04	0.07
Condition III	3.73	0.09
Condition IV	2.40	0.04

responses due to the heterogeneity of the background media, as the Green's function used in (5) and (6) includes the effects of multiple scattering and propagation velocity changes for each layer. The radar images obtained through the CSI-enhanced SAR approach are utilized in the post-CSI process to retrieve the complex permittivity of the object.

C. Results: Complex Permittivity Reconstruction

1) Relevance of Green's Functions: In this section, we investigate the effectiveness of the selected Green's function for the ROI-limited CSI, as described in Section II-D, by examining the dielectric profile reconstructions assuming a Case 1 object using four different Green's function patterns. Table III provides the definitions of each condition. The Green's functions for the data and state equations used in (3) and (4) are provided by the FDTD, CSI, or the analytical Hankel functions, respectively, where the wavenumber k_{B} in (11) is defined as that of the second layer. Note that Condition I corresponds to an ideal situation where both Green's functions are correctly given, while Condition IV assumes the most practical situation, where the FDTD-based forward solver is not introduced to generate a final reconstruction image. Fig. 10 shows the reconstruction results for relative permittivity and conductivity in each condition. Here, we set the iteration number of the CSI to 1000, and the background response from the multilayered medium, excluding the object, is completely eliminated by the FDTD calculation. To validate only the error factor of the Green's function, we provide the true ROI in each condition.

For a quantitative evaluation of the reconstruction image, we introduce the following root mean square error (RMSE) for

relative permittivity and conductivity

$$\mathrm{RMSE}_\epsilon = \frac{1}{N_{\mathrm{ROI}}} \sqrt{\sum_{i=1}^{N_{\mathrm{ROI}}} \left(\epsilon_i - \epsilon_{i,\mathrm{true}} \right)^2} \quad (15)$$

$$\mathrm{RMSE}_\sigma = \frac{1}{N_{\mathrm{ROI}}} \sqrt{\sum_{i=1}^{N_{\mathrm{ROI}}} \left(\sigma_i - \sigma_{i,\mathrm{true}} \right)^2} \quad (16)$$

where i denotes the index number of the ROI cell, ϵ_i and σ_i are the estimated relative permittivity and conductivity, respectively, while $\epsilon_{i,\mathrm{true}}$ and $\sigma_{i,\mathrm{true}}$ denote their true values. Table IV shows the RMSE_ϵ and RMSE_σ in each condition. These figures and results demonstrate that the reconstruction results do not significantly depend on each condition, whereas the RMSE_ϵ in Condition III is slightly worse in other conditions. These results demonstrate that the CSI-based estimation in Data equation and the Hankel function-based approximation in State equation offer a reliable estimate for the FDTD (referential data) based Green's function, even though the Hankel function assumes a homogeneous background. The reconstruction accuracy of the CSI for the data equations has also been discussed and validated in the literature [8], [9], aiming for the accuracy of radar imaging. Regarding the state equation, it is notable that using the homogeneous-based Green's function (Hankel function) provides almost the same level of accuracy as using the referential (FDTD-based) Green's function. It is worth noting that both RMSE_ϵ and RMSE_σ exceeds the true value $(\epsilon_r, \sigma) = (1.0, 0.001 \text{ S/m})$ under all conditions. This is because we set the background dielectric parameter $(\epsilon_r, \sigma) = (6.0, 0.1 \text{ S/m})$ in the ROI limitation scheme, which matches the second layer. This is due to the fact that the ROI is incorporated within the second layer. In addition, we tackle an intensely ill-posed
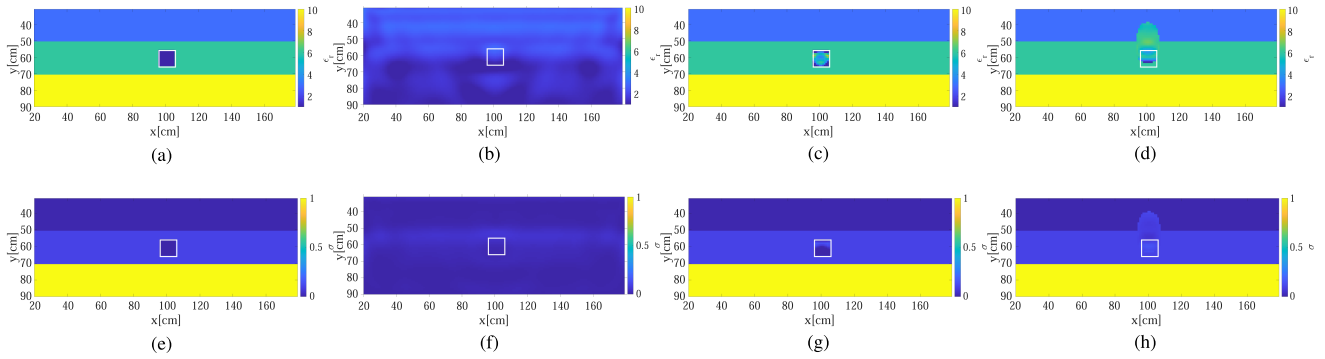
Fig. 11. Reconstruction results by each CSI method in Case 1. First line: Relative permittivity. Second line: Conductivity. (a) True. (b) Original CSI. (c) Proposed CSI (Given ROI). (d) Proposed CSI (Radar ROI). (e) True. (f) Original CSI. (g) Proposed CSI (Given ROI). (h) Proposed CSI (Radar ROI).
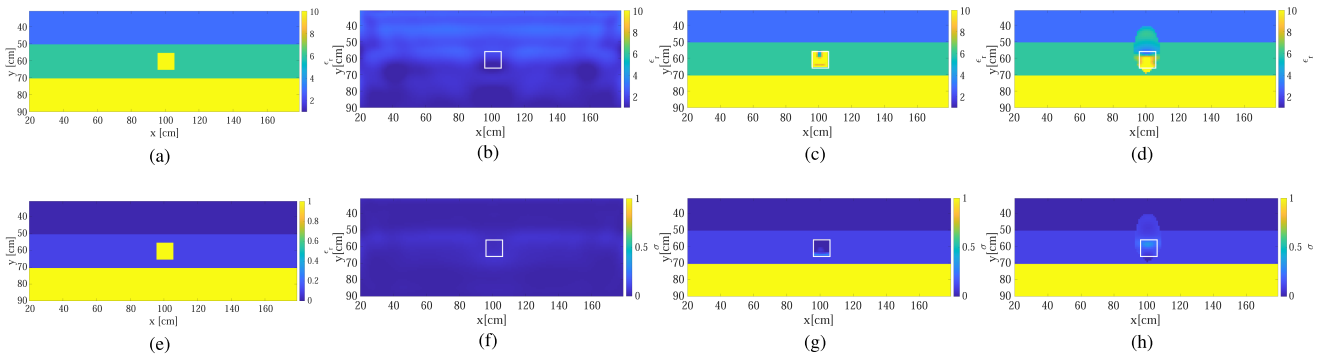

Fig. 12. Reconstruction results by each CSI method in Case 2. First line: Relative permittivity. Second line: Conductivity. (a) True. (b) Original CSI. (c) Proposed CSI (Given ROI). (d) Proposed CSI (Radar ROI). (e) True. (f) Original CSI. (g) Proposed CSI (Given ROI). (h) Proposed CSI (Radar ROI).

condition due to the limited illumination angle, and we assume a high contrast object, such as air in concrete material, even with the introduction of the ROI limitation scheme. Regardless, our proposed approach maintains substantial improvement from the initial RMSE $(\mathrm{RMSE}_\epsilon, \mathrm{RMSE}_\sigma) = (5.0, 0.099 \text{ S/m})$ by introducing the ROI limitation scheme.

2) Final Reconstruction Results: Figs. 11 and 12 show the final reconstruction results for Cases 1 and 2, respectively, in both the true ROI and radar-based ROI scenarios. Note that the Condition IV is used for all results in the proposed method. Here, the background response, which includes only scattered components from the multilayered medium excluding the object, is eliminated by the CSI-based background clutter generation, as described in (8). The iteration number of the CSI is 1000, and the threshold $\alpha = 0.2$, is set. Focusing on the case of the original CSI, without using the ROI limitation, the final reconstruction could not provide any meaningful reconstruction, and it was almost equivalent to the background air medium. On the contrary, the proposed CSI with ROI limitation offers more accurate results, especially for the true ROI scenario, by significantly reducing the number of unknowns. It is important to mention that the reconstruction results for the true ROI case in Fig. 11(c) and (g) are less accurate compared to those achieved in Fig. 10(d) and (h), even though condition (IV) was used in both scenarios. This discrepancy is because the background clutter in Fig. 10(d) and (h) is generated in FDTD, whereas it is estimated by the CSI outputs in Fig. 11(c) and (g), indicating that the background

TABLE V
RMSE FOR PERMITTIVITY AND CONDUCTIVITY RECONSTRUCTION IN CASE 1

	RMSE_ϵ	RMSE_σ S/m
Original CSI (w/o ROI limitation)	5.63	0.58
Proposed CSI (w/ true ROI)	3.25	0.12
Proposed CSI (w/ radar ROI)	2.63	0.07

TABLE VI
RMSE FOR PERMITTIVITY AND CONDUCTIVITY RECONSTRUCTION IN CASE 2

	RMSE_ϵ	RMSE_σ S/m
Original CSI (w/o ROI limitation)	5.68	0.58
Proposed CSI (w/ true ROI)	3.99	1.06
Proposed CSI (w/ radar ROI)	2.67	0.43

clutter could not be completely eliminated by the CSI. Although the results inn Fig. 10(d) and (h) assume that the background clutter is completely eliminated by the FDTD, namely, the ideal case, in the case of Fig. 11(c) and (g), these clutter components are reconstructed by the CSI and are estimated in (8). Thus, these comparisons demonstrate that the clutter response suppression performance directly affects the final reconstruction results, and similar discussions have been made in [8]. Tables V and VI show the RMSEs in Cases 1 and 2, respectively. These comparisons also demonstrate that our proposed scheme has a concrete superiority over the original CSI, even when using radar-based ROI estimation. Notably, as in the results in Figs. 11
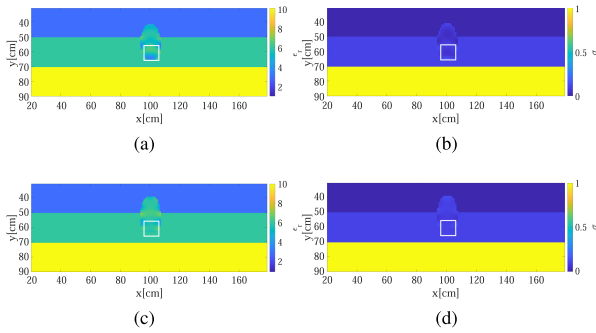
Fig. 13.   Reconstruction results in using single frequency data at 0.44 GHz, in assuming the proposed method with the radar-based ROI limitation. First line: Case 1. Second line : Case 2. (a) Relative permittivity. (b) Conductivity. (c) Relative permittivity. (d) Conductivity.

TABLE VII
RMSE IN USING SINGLE- AND MULTIFREQUENCY DATA IN THE PROPOSED
METHOD W/ THE RADAR-BASED ROI LIMITATION

	Case 1		Case 2	
	$\Re[\epsilon]$	$\Im[\epsilon]$	$\Re[\epsilon]$	$\Im[\epsilon]$
Multifrequency (59 samples)	2.63	0.07	2.63	0.43
Single frequency (1 sample)	3.14	0.08	3.14	0.54

TABLE VIII
COMPUTATIONAL COMPLEXITY AND ACTUAL RUN TIME IN EACH PROCESS

Method	Run time
Original CSI (w/o ROI limitation)	10 h
Proposed CSI (w/ radar ROI)	5 min

and 12, the accuracy of the radar image directly influences the reconstruction accuracy in the complex permittivity. While it is generally challenging to provide a complete estimate of the ROI using the radar image due to the limited spatial resolution or surface reflection effects from the ROI boundary, there are strategies to update the ROI using the CSI scheme as discussed in [27]. Nonetheless, the methods of providing the radar image as the ROI remains a critical issue and optimizing the inclusion of the ROI using the features of the inverse scattering method is an important future task.

As a reference, we present a case using only single frequency data for CSI reconstruction, where the proposed method with the radar-based ROI limitation scheme is applied. Fig. 13 displays the reconstruction results for Cases 1 and 2, where one frequency sample of 0.44 GHz, approximately the center frequency, is used for the CSI inversion. Table VII also compares the RMSEs between multiple (59 samples) and single frequency data for each case. As indicated by these results in Figs. 11 and 12, the reconstruction accuracy noticeably decreases compared with the multifrequency inversion, especially in Case 2, which involves a high contrast object. Therefore, the multifrequency inversion process is required to maintain reconstruction accuracy.

Here, the computational costs for each method is investigated as follows. Table VIII presents the actual computational time, using an Intel Xeon Gold 5218 x4 processor with 3072 GB RAM, and it shows that our proposed method remarkably

TABLE IX
RMSE IN EACH SNR LEVEL

	Case 1		Case 2	
	$\Re[\epsilon]$	$\Im[\epsilon]$	$\Re[\epsilon]$	$\Im[\epsilon]$
SNR = ∞ dB	2.63	0.07	2.63	0.43
SNR = 30 dB	2.86	0.08	3.02	0.45
SNR = 20 dB	2.87	0.07	3.36	0.50

reduces the computational cost due to the massive reduction in the number of unknowns, from 9600 to 300. Moreover, the Green's function in data and state equations is calculated by the CSI and the analytical form, such as the Hankel function. This considerably reduces the necessary computational cost required in each iteration step, which is advantageous over the method using FDTD-based Green's function generation.

D. Sensitivity to Noise

This section presents the reconstruction results in the presence of additive noise. Herein, white Gaussian noise components are directly added to the recorded total fields in the time domain. The signal-to-noise ratio (SNR) is defined as the ratio of maximum signal power to noise power. Notably, the signal only included the reflection response from the buried object. Thus, each surface reflection from stratified media is excluded in the SNR calculation. We investigated two scenarios with SNR levels of 30 dB and 20 dB, which are attainable in realistic situations as per [35], [36]. Figs. 14 and 15 display the reconstruction images for Cases 1 and 2 for the CSI-enhanced SAR images as well as the relative permittivity and conductivity provided by the proposed ROI-limited CSI at SNR levels of 30 and 20 dB, respectively. In the proposed CSI, we assumed the radar-based ROI with Condition IV, thereby facilitating comparison with the results in Figs. 11 and 12(d) and (h) as the noise-free case. In addition, Table IX shows the RMSEs for each obtained image. Focusing on the CSI-enhanced SAR images, it is apparent that the provided images are nearly identical to those in the noise-free situation (see Figs. 8 and 9) for both cases. This similarity is due to the SAR's image generation, which relies on a coherent integration process as in (7), significantly suppressing the noise component. In contrast, the reconstruction of relative permittivity and conductivity encounters inaccuracy due to noise, particularly for 20 dB in Cases 1 and 2. Meanwhile, the results for 30 dB almost mirror those provided in the noise-free situation. To improve the reconstruction accuracy in lower SNR cases, we may need to employ a noise-reduction filter, such as matched filtering, as a preprocessing step in the CSI-based reconstruction scheme.

E. Further Discussions

This section discusses the proposed method's practicability, applicability, and potential limitations in real-world applications. It is important to note that applying this method to a real scenario necessitates an effective calibration process, converting the experimental data into a simulation data. Various approaches
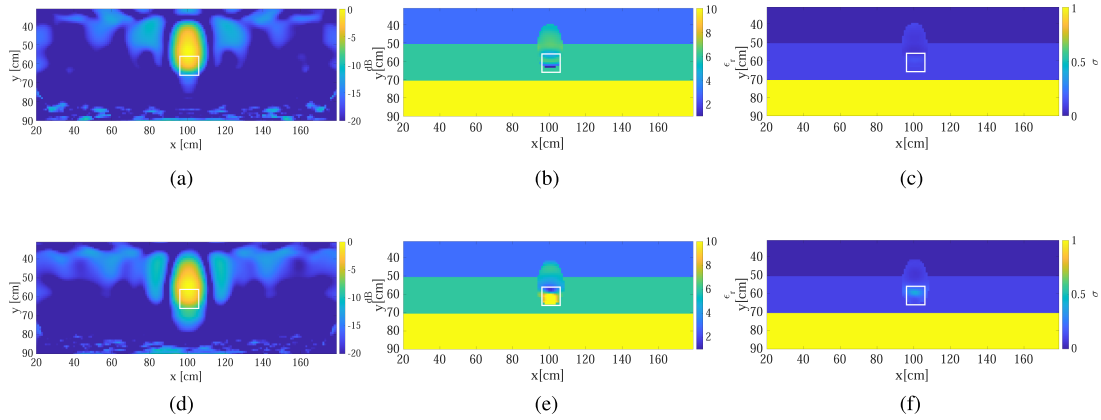
Fig. 14. Reconstruction results in each CSI method at Case 1 in SNR of 30 dB. First line: Case 1. Second line : Case 2. (a) CSI enhanced SAR. (b) Proposed CSI (Radar ROI), Relative permittivity. (c) Proposed CSI (Radar ROI), Conductivity. (d) CSI enhanced SAR. (e) Proposed CSI (Radar ROI), Relative permittivity. (f) Proposed CSI (Radar ROI), Conductivity.
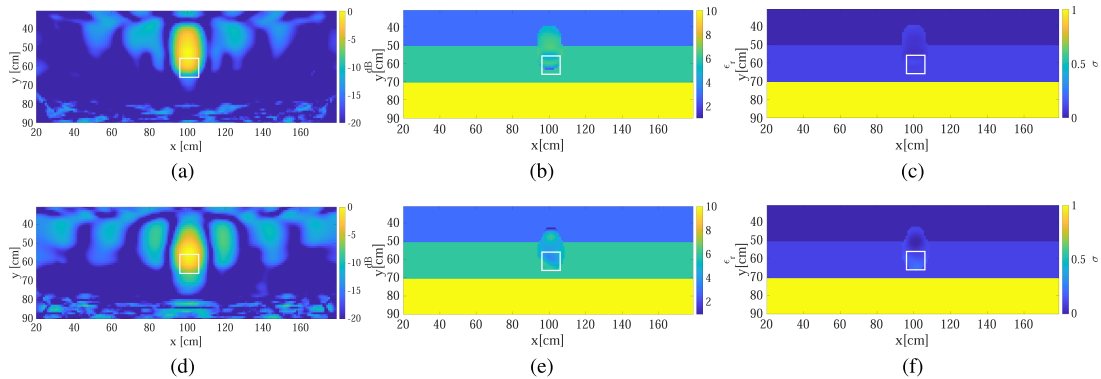

Fig. 15. Reconstruction results in each CSI method at Case 1 in SNR of 20 dB. First line: Case 1. Second line : Case 2. (a) CSI enhanced SAR. (b) Relative permittivity. (c) Conductivity. (d) CSI enhanced SAR. (e) Relative permittivity. (f) Conductivity.

have been developed for this calibration, including linear transfer function-based methods [37], [38] and deep learning-based processing [39], [40]. However, it is challenging to fully convert experimental data into ideal simulation data as it requires accurate parameters, such as dielectric property, dimensions, or structures of antennas, or other components, such as cable or insertion loss of a vector network analyzer or radar module. Our previous study [41] demonstrated the successful CSI-based complex permittivity reconstruction in a nondestructive testing model using the L-band UWB radar module, comparable to those assumed in this GPR model. Consequently, future efforts should focus on applying an effective calibration approach using a real radar module and stratified ground media.

It should also be noted that unlike other inverse scattering approaches, our proposed method does not require the forward solver to generate the Green's functions for a heterogeneous stratified model. In other words, the Green's function in the data equation can be provided by the optimized total fields from the pre-CSI process, and the function in the state equation is approximated as an analytical Hankel function. This approximation effect is deemed acceptable in the reconstruction results. These advantages enhance the applicability of our proposed method to realistic scenarios.

IV. CONCLUSION

This article presented the radar image enhanced complex permittivity retrieval method of an object buried in multilayered ground media using GPR investigation. The method is based on the use of the specific inverse scattering method known as CSI, which provides the total fields in the ROI as optimization outputs. These total fields are then used to generate an accurate Green's function model in heterogeneous background media, which enhances the synthetic aperture-based radar image. The resulting radar image is then used in the post-CSI processing to improve the reconstruction accuracy of the complex permittivity of the buried object by significantly reducing the number of unknowns through ROI limitation. The proposed scheme is validated through 2-D FDTD numerical analysis, which demonstrates its ability to enhance the reconstruction accuracy in different soil layers, including an air, and a wet clay target. Moreover, the proposed method is computationally efficient due to the use of the CSI output and analytical Hankel function for Green's function used in the CSI cost function. Interestingly, there are promising inverse scattering approaches that eliminate the need for an iterative use of the forward solver, such as, e.g., [42], [43], [44]. Thus, our proposed scheme can be extended to integrate

with these algorithms, provided that accurate total fields in the ROI are available. Future work includes an experimental study with a 3-D model extension.

REFERENCES

[1] Japan Ministry of Land, Infrastructure, Transport and Tourism, Council for Social Infrastructure Development, 2017. Accessed: Dec. 13, 2020. [Online]. Available: https://www.mlit.go.jp/policy/shingikai/kanbo08_sg_000106.html

[2] C. Özdemir, F. Demirci, E. YiLit, and B. Yilmaz, "A review on migration methods in B-scan ground penetrating radar imaging," *Math. Problems Eng.*, vol. 13, pp. 1607–1620, Jul. 1997.

[3] N. Smitha, D. R. U. Bharadwaj, S. Abilash, S. N. Sridhara, and V. Singh, "Kirchhoff and F-K migration to focus ground penetrating radar images," *Int. J. Geo-Eng.*, vol. 7, no. 4, pp. 1–12, 2016.

[4] M. González-Díaz, M. García-Fernández, Y. Álvarez-López, and F. Las-Heras, "Improvement of GPR SAR-Based techniques for accurate detection and imaging of buried objects," *IEEE Trans. Instrum. Meas.*, vol. 69, no. 6, pp. 3126–3138, Jun. 2020.

[5] J. I. Halman, K. A. Shubert, and G. T. Ruck, "SAR processing of ground-penetrating radar data for buried UXO detection: Results from a surface-based system," *IEEE Trans. Antennas Propag.*, vol. 46, no. 7, pp. 1023–1027, Jul. 1998.

[6] M. Fallahpour, J. T. Case, M. Ghasr, and R. Zoughi, "Piecewise and wiener filter-based SAR techniques for monostatic microwave imaging of layered structures," *IEEE Trans. Antennas Propag.*, vol. 62, no. 1, pp. 282–294, Jan. 2014.

[7] W. Zhang and A. Hoorfar, "MIMO ground penetrating radar imaging through multilayered subsurface using total variation minimization," *IEEE Trans. Geosci. Remote Sens.*, vol. 57, no. 4, pp. 2107–2115, Apr. 2019.

[8] Y. Yamauchi and S. Kidera, "Inverse scattering enhanced synthetic aperture imaging for multi-layered ground media," in *Proc. Int. Symp. Antennas Propag.*, 2022, pp. 225–226.

[9] Y. Yamauchi and S. Kidera, "Contrast source inversion enhanced synthetic aperture approach for microwave multi-layered subsurface imaging," *IEEE Trans. Antennas Propag.*, vol. 71, no. 9, pp. 7538–7552, Sep. 2023.

[10] E. Pettinelli et al., "GPR response from buried pipes: Measurement on field site and tomographic reconstructions," *IEEE Trans. Geosci. Remote Sens.*, vol. 47, no. 8, pp. 2639–2645, Aug. 2009.

[11] F. Soldovieri, J. Hugenschmidt, R. Persico, and G. Leone, "A linear inverse scattering algorithm for realistic GPR applications," *Near Surf. Geophys.*, vol. 5, pp. 29–41, Feb. 2007.

[12] G. Leone and F. Soldovieri, "Analysis of the distorted Born approximation for subsurface reconstruction: Truncation and uncertainties effects," *IEEE Trans. Geosci. Remote Sens.*, vol. 41, no. 1, pp. 66–74, Jan. 2003.

[13] N. Anselmi, L. Poli, G. Oliveri, and A. Massa, "Iterative multiresolution Bayesian CS for microwave imaging," *IEEE Trans. Antennas Propag.*, vol. 66, no. 7, pp. 3665–3677, Jul. 2018.

[14] M. Salucci et al., "A multi-resolution computational method to solve highly non-linear inverse scattering problems," *J. Phys.: Conf. Ser.*, vol. 1476, 2020, Art. no. 012002.

[15] M. Salucci, L. Poli, N. Anselmi, and A. Massa, "Multifrequency particle swarm optimization for enhanced multiresolution GPR microwave imaging," *IEEE Trans. Geosci. Remote Sens.*, vol. 55, no. 3, pp. 1305–1317, Mar. 2017.

[16] N. Anselmi, L. Poli, G. Oliveri, and A. Massa, "Iterative multi-resolution Bayesian CS for microwave imaging," *IEEE Trans. Antennas Propag.*, vol. 66, no. 7, pp. 3665–3677, Jul. 2018.

[17] G. Oliveri, L. Poli, and A. Massa, "On the exploitation of the a-priori information through the Bayesian compressive sensing for microwave imaging," in *Proc. 6th Eur. Conf. Antennas Propag.*, 2012, pp. 1502–1503.

[18] P. M. van den Berg and R. E. Kleinman, "A contrast source inversion method," *Inverse Problems*, vol. 13, pp. 1607–1620, Jul. 1997.

[19] R. F. Bloemenkamp, A. Abubakar, and P. M. van den Berg, "Inversion of experimental multi-frequency data using the contrast source inversion method," *Inverse Problems*, vol. 17, pp. 1611–1622, 2001.

[20] P. M. van Den Berg and A. Abubakar, "Contrast source inversion method: State of the art," *Prog. Electromagn. Res.*, vol. 34, pp. 189–218, 2001.

[21] P. M. van den Berg, A Abubakar, N. V. Budko, and R. F. Remis, "Imaging and inversion of buried objects using GPR," in *Proc. IEEE Int. Geosci. Remote Sens. Symp.*, 2001, pp. 1377–1380.

[22] S. Sun, B. J. Kooij, and A. G. Yarovoy, "Linearized 3-D electromagnetic contrast source inversion and its applications to half-space configurations," *IEEE Trans. Geosci. Remote Sens.*, vol. 55, no. 6, pp. 3475–3487, Jun. 2017.

[23] R. Marklein, J. Miao, M. Rhaman, and K. J. Langenberg, "Inverse scattering and imaging in NDT: Recent applications and advances," in *Proc. 9th Eur. Conf. NDT*, 2006.

[24] L. P. Song, Q. H. Liu, F. Li, and Z. Q. Zhang, "Reconstruction of three-dimensional objects in layered media: Numerical experiments," *IEEE Trans. Antennas Propag.*, vol. 53, no. 4, pp. 1556–1561, Apr. 2005.

[25] M. A. Ali and M. Moghaddam, "3D nonlinear super-resolution microwave inversion technique using time-domain data," *IEEE Trans. Antennas Propag.*, vol. 58, no. 7, pp. 2327–2336, Jul. 2010.

[26] Y. Yamauchi and S. Kidera, "Contrast source inversion for objects buried into multi-layered media for subsurface imaging applications," *IEICE Trans. Electron.*, vol. E106.C, 2023, Art. no. 2022ECS6008.

[27] S. Takahashi, K. Suzuki, T. Hanabusa, and S. Kidera, "Microwave subsurface imaging method by incorporating radar and tomographic approaches," *IEEE Trans. Antennas Propag.*, vol. 70, no. 11, pp. 11009–11023, Nov. 2022.

[28] S. Takahashi and S. Kidera, "Incorporation algorithm with RPM and DBIM in Bayesian framework for microwave non-destructive testing," in *Proc. URSI Asia-Pacific Radio Sci. Conf.*, 2019, pp. 1–4.

[29] M. Benedetti, M. Donelli, D. Lesselier, and A. Massa, "A two-step inverse scattering procedure for the qualitative imaging of homogeneous cracks in known host media—Preliminary results," *IEEE Antennas Wireless Propag. Lett.*, vol. 6, pp. 592–595, 2007.

[30] O. Dorn and D. Lesselier, "Level set methods for inverse scattering," *Inverse Problems*, vol. 22, 2006, Art. no. R67.

[31] H. Sato and S. Kidera, "ROI limited unknowns reduction-based contrast source inversion for microwave breast imaging," *IEEE Antennas Wireless Propag. Lett.*, vol. 19, no. 12, pp. 2285–2289, Dec. 2020.

[32] M. Salucci, L. Poli, N. Anselmi, and A. Massa, "Multi-scale compressive processing for inverse scattering within the contrast source formulation," in *Proc. IEEE Int. Symp. Antennas Propag. USNC-URSI Radio Sci. Meeting*, 2019, pp. 1017–1018.

[33] C. Curtis and E. Fear, "Beamforming in the frequency domain with applications to microwave breast imaging," in *Proc. 8th Eur. Conf. Antennas Propag.*, 2014, pp. 72–76.

[34] J. B. Rhebergen, H. A. Lensen, P. B. W. Schwering, G. R. Marín, and J. M. H. Hendrickx, "Soil moisture distribution around land mines and the effect on relative permittivity," *Proc. SPIE*, vol. 4742, pp. 269–280, Aug. 2002.

[35] J. Zhang, S. Ye, Y. Lin, X. Liu, and G. Fang, "A modified model for quasi-monostatic ground penetrating radar," *IEEE Geosci. Remote Sens. Lett.*, vol. 17, no. 3, pp. 406–410, Mar. 2020.

[36] J. Li, C. Le Bastard, Y. Wang, G. Wei, B. Ma, and M. Sun, "Enhanced GPR signal for layered media time-delay estimation in Low-SNR scenario," *IEEE Geosci. Remote Sens. Lett.*, vol. 13, no. 3, pp. 299–303, Mar. 2016.

[37] M. Ostadrahimi et al., "Analysis of incident field modeling and incident/scattered field calibration techniques in microwave tomography," *IEEE Antennas Wireless Propag. Lett.*, vol. 10, pp. 900–903, 2011.

[38] M. Salucci et al., "2-D TM GPR imaging through a multiscaling multifrequency approach in Lp spaces," *IEEE Trans. Geosci. Remote Sens.*, vol. 59, no. 12, pp. 10011–10021, Dec. 2021.

[39] A. Fedeli, "Microwave tomography with LSTM-Based processing of the scattered field," *IEEE Open J. Antennas Propag.*, vol. 2, pp. 213–223, 2021.

[40] T. Hanabusa, T. Morooka, and S. Kidera, "Deep-learning-based calibration in contrast source inversion based microwave subsurface imaging," *IEEE Geosci. Remote Sens. Lett.*, vol. 19, no. 19, Apr. 2022, Art. no. 3006805.

[41] K. Suzuki and S. Kidera, "Radar enhanced contrast source inversion method for microwave nondestructive evaluation," in *Proc. Int. Symp. Antennas Propag.*, 2022, pp. 223–224.

[42] K. Xu, Y. Zhong, and G. Wang, "A hybrid regularization technique for solving highly nonlinear inverse scattering problems," *IEEE Trans. Microw. Theory Techn.*, vol. 66, no. 1, pp. 11–21, Jan. 2018.

[43] Y. Zhong and X. Chen, "An FFT twofold subspace-based optimization method for solving electromagnetic inverse scattering problems," *IEEE Trans. Antennas Propag.*, vol. 59, no. 3, pp. 914–927, Mar. 2011.

[44] K. Xu, Y. Zhong, X. Chen, and D. Lesselier, "A fast integral equation-based method for solving electromagnetic inverse scattering problems with inhomogeneous background," *IEEE Trans. Antennas Propag.*, vol. 66, no. 8, pp. 4228–4239, Aug. 2018.

Yoshihiro Yamauchi received the B.E. degree in communication engineering and informatics from the University of Electro-Communications, Tokyo, Japan, in 2021 and the M.E. degree in informatics and communication engineering from the University of Electro-Communications, Tokyo, Japan, in 2023.

He joined Capgemini Japan K.K., Tokyo, Japan, in 2023.

Shouhei Kidera (Senior Member, IEEE) received the B.E. degree in electrical and electronic engineering from Kyoto University, Kyoto, Japan, in 2003 and the M.I. and Ph.D. degrees in informatics from Kyoto University, Kyoto, Japan, in 2005 and 2007, respectively.

In 2009, he joined as an Assistant Professor with the University of Electro-Communications, Tokyo, Japan, where he is currently a Full Professor with the Graduate School of Informatics and Engineering, University of Electro-Communications, Tokyo, Japan. He was with the Cross-Disciplinary Electromagnetics Laboratory, University of Wisconsin Madison, Madison, WI, USA, as the visiting Researcher in 2016. He was a Principal Investigator of the PRESTO Program of Japan Science and Technology Agency (JST) from 2017 to 2021. His current research interests include advanced radar signal processing or electromagnetic inverse scattering issue for ultrawideband (UWB) three-dimensional sensor or biomedical applications.

Dr. Kidera was the recipient of the 2012 Ando Incentive Prize for the Study of Electronics, 2013 Young Scientist's Prize by the Japanese Minister of Education, Culture, Sports, Science and Technology (MEXT), and 2014 Funai Achievement Award, 2022 KDDI Foundation Award, Contribution Award, and 2023 RIEC Award. He is a senior member of the Institute of Electronics, Information, and Communication Engineers of Japan (IEICE), and the International Union of Radio Science (Union Radio-Scientifique Internationale, URSI), and a member of the Institute of Electrical Engineering of Japan (IEEJ), and the Japan Society of Applied Physics (JSAP).